Materials Science & Engineering A 727 (2018) 170–176

Contents lists available at ScienceDirect

Materials Science & Engineering A

journal homepage: www.elsevier.com/locate/msea

Relating porosity to fatigue failure in additively manufactured alloy 718

Luke Sheridan[a,b,*], Onome E. Scott-Emuakpor[a], Tommy George[a], Joy E. Gockel[b]

[a] Air Force Research Laboratory, Aerospace Systems Directorate,Turbine Engine Structural Integrity Branch, 2130 Eighth St., Rm 136, Wright Patterson AFB, Dayton, OH 45433, USA

[b] Mechanical and Materials Engineering, Wright State University, 3640 Colonel Glenn Hwy, Dayton, OH 45435, USA

ARTICLE INFO

Keywords:
Additive manufacturing
Alloy 718
Fatigue
Crack growth rate
Porosity

ABSTRACT

Additive manufacturing (AM) has the potential to revolutionize the way parts are designed and manufactured; however, AM also produces defects that influence the performance of the components. In order to ensure the quality of the manufactured parts, the processing-structure-property-performance (PSPP) relationship must be understood. In this study, the porosity created during the AM process is investigated, and its influence on performance is quantified with respect to the PSPP framework. Test specimens were fabricated with different processing pedigrees, and the porosity populations within each specimen was characterized. The fatigue life of the specimen was predicted based on the size and location of porosity using a fatigue crack growth approach. Results show that the fatigue life can be successfully predicted, when the appropriate crack growth behavior is used. The insight gained in this study will inform future AM fatigue studies and will lay the groundwork for design and qualification of fracture-critical AM components.

1. Introduction

The versatility of AM processes allows for re-evaluation of current practices to produce cutting edge, weight-reducing designs while reducing costs and material waste. Although the benefits of AM make it attractive to the defense and aerospace industries for maintenance, sustainment, and innovation both in deployed and domestic environments [1], there are many complex facets that need to be addressed before AM may be considered a viable manufacturing process for fracture-critical components. Critical structures in turbine engines experience cyclic stresses because of aero-driven vibration, blade rubs, and rotordynamic phenomena. Therefore, qualification techniques and rejection criteria must be developed to fully characterize failure-inducing material defects in AM components before they may be leveraged in fracture-critical applications. Additionally, the model for the relationship between processing, structure, properties and performance (PSPP) must be developed to efficiently facilitate best practices for consistent AM components.

Many studies have shown that material properties of AM materials differ significantly from wrought materials [2], and AM components may exhibit notable scatter due to the large number of variables that influence the PSPP outcomes [3]. It is well known that the processing of an AM material from raw powder to final heat treatment dictates the material performance in a given application [4,5]. The thermal history of an AM component has bearing on a wide range of material characteristics including microstructure [6–8], residual stress [9], and porosity [10,11]. Porosity is known to dictate fatigue performance in many traditional materials. In casting, micro-porosity and shrinkage porosity were shown to act as stress concentrators which lead to crack initiation and failure [12,13], and quantification of porosity distributions was shown to provide sufficient information to predict component life using statistical methods [14,15]. Similarities in porosity observed in both casting and AM materials indicate that historical methods may be used to characterize the porosity content in AM components.

Primary processing parameters (PPP) such as, but not limited to, beam power, raster speed, and hatch spacing have been varied to explore the mechanism for developing porosity in AM. It has been shown that different types of porosity are developed by manipulating these PPPs, and that controlling the quantity, size, and morphology of porosity populations can be achieved [10]. This work utilizes four PPPs (power, speed, hatch spacing, and layer thickness) and multiple scan strategies that are known to influence porosity content, and explores the PPP space to further develop the understanding of the PSPP framework in relation to fatigue life of AM components. The parameters are varied to obtain various porosity distributions and the porosity is subsequently related to the fatigue life.

* Corresponding author at: Air Force Research Laboratory, Aerospace Systems Directorate,Turbine Engine Structural Integrity Branch, 2130 Eighth St., Rm 136, Wright Patterson AFB, Dayton, OH 45433, USA.
E-mail address: luke.sheridan.1@us.af.mil (L. Sheridan).

https://doi.org/10.1016/j.msea.2018.04.075
Received 1 March 2018; Received in revised form 17 April 2018; Accepted 18 April 2018
Available online 24 April 2018
0921-5093/ Published by Elsevier B.V.

Nomenclature

PSPP	Processing, Structure, Properties, Performance
PPP	Primary Processing Parameter
CL	Concept Laser
CM	Continuous Meander Scan Strategy
SM	Stripped Meander Scan Strategy
IM	Island Meander Scan Strategy
EDM	Electron Discharge Machine
C	Crack growth constant
n	Crack growth constant
Y	Stress intensity shape factor
a_1	Initial crack length
a_2	Final crack length
a_c	Critical crack length
$\Delta\sigma$	Peak to peak stress amplitude
R	Load Ratio

2. Materials and methods

This paper brings together data from two different experiments that will provide further insight into the PSPP model for AM materials from different material and processing pedigrees. In the first experiment, three scanning strategies (SS) were used, and in the second experiment, three PPP settings were used to explore the effect of processing changes on the formation of porosity. In both of these experiments, the internal porosity was measured using computed tomography (CT), and predictions were made based on these observations and the application of crack growth theory. The CT measurements were obtained using a North Star Imaging X-View X-50 machine. A summary of the experimental design is provided in Table 1 where A,B, and C denote the three SS and PPP settings for their respective experiment.

2.1. Experiment 1: Scan strategies

The components produced for the SS study were manufactured using a Concept Laser™ (CL) M2 Cusing laser powder bed fusion machine. Alloy 718 powder was used to construct five rectangular bars on a 316 L stainless steel plate. Three different scan strategies were used including Continuous Meander (CM), Striped Meander (SM), and Island Meander (IM).

In CM, the beam scans across the entire part in a continuous raster while in SM, a strip of width 5 mm creates multiple raster patterns across the width of the part. In IM, 5 mm squares are melted at random across the entire component cross-section. For each powder layer, CM and IM undergo a 1 mm layer shift and a 90 degree layer rotation. CL's layer exposure technique also incorporates a skin and core strategy where the skin and core regions are exposed differently. The skin is exposed every layer under one PPP setting, and the core is exposed every other layer under a different PPP setting. The core material controls the fatigue performance of the component because the skin material is machined off, but it must be noted that the 50 μm noted in Table 1 is actually two 25 μm layers of powder that have been deposited on top of each other and subsequently exposed.

For this experiment, the core beam settings, power, speed, hatch spacing, and laser spot size, were held constant for each component as shown in Table 1. The components were stress relieved on the plate according to ASTM F3055 [16], wire electron discharge machined (EDM) from the plate, and solution annealed and aged according to AMS 2774 [17]. Each component was machined into a round fatigue bar within the ASTM E466 standard [18], low stress ground to final dimensions, and electro-polished to a mirror finish. The machining removed the entire skin region in the gage section and left the core material for testing. The gage section of each specimen underwent CT measurements with a 14 μm/voxel resolution, and the ImageJ (v. 1.5 H) software package [19] was used to process these images and to measure the observed pores.

2.2. Experiment 2: Primary processing parameters

The second experiment was performed using an EOS M290 laser powder bed fusion machine. Alloy 718 powder was used to construct eight rectangular bars on a 316 L stainless steel plate. This experiment was to develop a relationship between PPPs (power, speed, hatch), porosity content, and resulting fatigue life of AM components. Three different PPP combinations (see Table 1) were specified. For this experiment the stripes scan strategy was used for all bars and the beam settings were modified. The porosity in the gage section was measured using CT, and the images were analyzed via ImageJ using the same procedure as the Scan Strategy Experiment.

2.3. Raw material and processing

Two different powder pedigrees were used for the two experiments. The powder used in the scan strategy study had been reused approximately 10 times at the time of the build while the powder used in the PPP study had been lightly reused (< 5 times). The powder morphology for both batches was observed in a NanoScience Phenom Pro scanning electron microscope. Irregularly shaped powder particles with multiple satellites were observed in both powder batches (Fig. 1). Diligent sieving procedures and enclosed powder hoppers ensured that large powder particles were removed and the contamination level was kept low for both batches.

Post process chemistry analyses were performed for five samples from both experiments, and the chemical composition for each of those specimens was determined using wet chemical analysis (Table 2). A representative specimen for PPP-A was not available for chemical testing at the time of the procedure, so this measurement was omitted from consideration. The chemistry of the components for each experiment were found to be within the specifications for alloy 718. Due to the consistency of the chemical composition for each of the tested components, it is assumed that the PPP-A's chemistry is consistent with the other components.

Table 1
Overview of experiment.

Machine	Concept laser M2 cusing			EOS M290		
Setting name	SS-A	SS-B	SS-C	PPP-A	PPP-B	PPP-C
Power	370 W			285 W		
Velocity	700 mm/s			1000 mm/s	1150 mm/s	1400 mm/s
Hatch Spacing	0.13 mm			0.120 mm	0.110 mm	0.055 mm
Layer Thickness	0.050 mm			0.020 mm		
Scan Strategy	Continuous	CL Stripped	Island	EOS Striped		

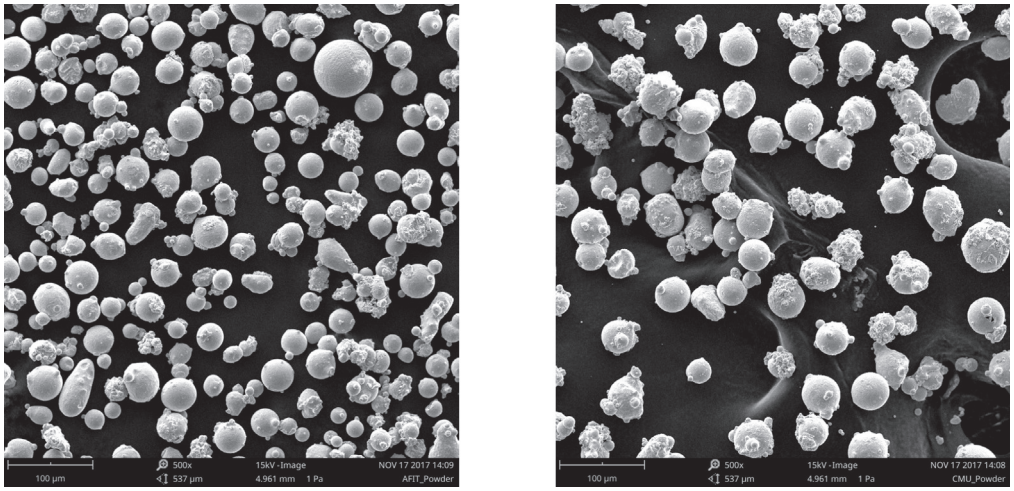

(a) (b)

Fig. 1. Powder samples obtained from a) the SS Experiment and b) PPP Experiment.

2.4. Fatigue life prediction

Murakami [20] showed that a pore or inclusion within a material was analogous to a small crack so that the stress intensity factor ΔK_I of an interior pore could be represented by

$$\Delta K_{I,i} = 0.5\sigma\sqrt{\pi\sqrt{A_i}} \tag{1}$$

and a surface pore by

$$\Delta K_{I,j} = 0.65\sigma\sqrt{\pi\sqrt{A_j}} \tag{2}$$

where A_i and A_j are the projected area of any bulk and surface pore respectively. According to Murakami a pore is a surface pore if $\sqrt{A}/e_0 > 0.8$ where e_0 is the distance of the pore's centroid to the free edge of the component. [20]. Growth of the pore into a long crack will develop under cyclic load to some critical effective diameter (a_c), which will cause the component to fail. It is well known that fatigue crack growth rate ($\frac{da}{dN}$) depends on the cyclic stress intensity factor so that

$$\frac{da}{dN} = C(\Delta K_I)^n \tag{3}$$

Because ΔK_I is a function of crack length (a), like terms may be isolated, and each side of the equation may be integrated to give a general equation for fatigue life prediction based on initial crack length and final crack length.

$$N_f = \frac{1}{CY\Delta\sigma\sqrt{\pi}} * \frac{a_2^{-n/2+1} - a_1^{-n/2+1}}{-n/2+1} \tag{4}$$

where C and n are crack growth constants, Y is the stress intensity shape factor, a_1 is the initial crack length, and a_2 is the final crack length. Konecna et al. [21] recently showed that the crack growth rate of selective laser melted Inconel 718 having undergone hot isostatic pressing (HIP) procedures may be represented using the parameters $(C, n) = (4.54*10^{-11}, 2.3)$, so

$$N_{f,bulk} = \frac{a_1^{-0.15} - a_c^{-0.15}}{(0.15)(4.54*10^{-11})(0.5\Delta\sigma\sqrt{\pi})^{2.3}} \tag{5}$$

and

$$N_{f,surf} = \frac{a_1^{-0.15} - a_c^{-0.15}}{(0.15)(4.54*10^{-11})(0.65\Delta\sigma\sqrt{\pi})^{2.3}} \tag{6}$$

where a_1 is the initial effective pore diameter and a_c is the critical crack size at which the component will fail. This crack size value is defined as the length of the crack required to exceed the bearing strength of the material under a given load. For application of the crack-growth based life prediction method presented above to larger components, the critical crack size may be defined as the minimum crack size that will surpass either the bearing strength or the critical fracture toughness of the material.

During the fatigue life prediction, several assumptions were made. First, it was assumed that the largest defects observed via CT were representative of "worst-case" defects and would therefore drive fatigue failure of the component. Second, although the material in these experiments underwent different post-processing procedures from the previously published crack growth data [21], it was assumed that the crack growth behavior for all the components in this study would be similar to those previously reported. Finally, it was assumed that pore shape did not play a large role in determining the failure location within the component. This assumption was made due to the large number of spherical pores that these components exhibited. Lack of fusion defects subjected to a load may experience orientation dependent stress states, but for this experiment, the majority of the lack-of-fusion porosity contained in these specimens were small in comparison to the spherical defects, and they were oriented parallel to the loading direction which greatly reduced their stress concentrations.

Table 2
Chemical analysis of manufactured components.

	Al	B	Cr	Cu	Fe	Mn	Mo	Ni + Co	Nb + Ta	P	Ti	C	S
Nominal	0.5	< 0.006	19.00	< 0.3	18.00	< 0.35	3.05	Bal.	5.15	< 0.015	0.9	< 0.08	0.015
SS-A	0.51	< 0.002	19.68	0.060	18.55	0.055	3.19	Bal.	5.09	3.1e-3	1.09	0.037	2.30e-3
SS-B	0.55	< 0.002	19.35	0.062	18.36	0.013	3.21	Bal.	5.06	3.1e-3	1.07	0.036	2.60e-3
SS-C	0.54	< 0.002	19.58	0.061	18.34	0.056	3.24	Bal.	5.04	3.3e-3	1.06	0.036	2.45e-3
PPP-B	0.51	< 0.002	18.83	0.069	18.34	0.059	3.25	Bal.	5.06	3.3e-3	1.15	0.039	3.01e-3
PPP-C	0.52	< 0.002	18.24	0.064	18.20	0.020	3.24	Bal.	5.08	3.2e-3	1.14	0.037	3.11e-3

2.5. Fatigue testing

After quantifying the porosity in each specimen, load controlled, axial, room temperature fatigue tests were performed with a 100 kN MTS servo-hydraulic load frame. The maximum stress was limited to 900 MPa with a load ratio $R = 0.1$. Each specimen was fatigued at a linear frequency of 20 Hz until catastrophic failure occurred.

3. Results and discussion

3.1. Experiment 1

Using image slices from the CT measurements, the porosity data were collected. For each pore, the cross-sectional area was measured, and the effective diameter was calculated. For all the slices the collective pore diameter distribution was constructed. Diameters under 14 μm were removed from consideration to account for image processing artifacts and to discard any pores smaller than the threshold crack length obtained from Konecna. Furthermore, it is assumed that fatigue failure is driven by "worst-case" phenomena, so the largest pores are expected to have the most significant effect.

Examination of the pore measurements show that the porosity content drastically changes with different scan strategies. This is illustrated in Fig. 2 which shows the cumulative distribution function (CDF) of the pore size for each component. This data shows the percent likelihood that a certain pore size will occur within a given specimen. The red lines represent SS-A, the blue lines represent SS-B, and the green line represents SS-C. The same scan strategies group together with SS-A exhibiting the smallest average porosity and SS-B exhibiting the largest average porosity. Qualitative observations show that in general, the pore morphologies for all of the components were large and spherical which indicates that over-melting of the material may have occurred because of non-optimal PPPs. The component porosity content indicates that the components manufactured via the SS-A strategy will perform better than components manufactured via the other two scan strategies because of the smaller maximum pore size. In addition, the average CT slice density was calculated for each component. Components manufactured with the same scan strategy exhibited similar slice density distributions, and although the average density for each component was above 99.9%, significant differences among the scan strategies were observed such that SS-A exhibited the highest average density, and SS-B exhibited the lowest average density. In comparison, the average density and the pore size distributions correlate with each other which is intuitive. The fatigue life prediction was calculated based on the maximum stress intensity calculated for each component. The pore diameter producing this stress intensity value was applied to Eq. (5) or Eq. (6) depending on its distance from the surface. When comparing the predicted life to the actual life from fatigue testing, it was observed that estimating the fatigue life based on the largest stress intensity criteria gave predictions that consistently lie within a 2x scatter band when compared to the actual component life. More specifically, it is seen from Fig. 3 that SS-A performed the best while SS-B and SS-C performed at levels similar to each other. This behavior indicates that the life prediction method based on the porosity diameter distributions measured from the gage section of each component provides an accurate prediction of fatigue life that can be leveraged to qualify components and identify design criteria for AM components.

3.2. Experiment 2

A similar analysis, as described above, was performed for the PPP study components to test whether the life prediction method can be used for components with different processing pedigree. The cross-sectional area for every pore throughout the gage section was measured from CT slices, and the pores under 14 μm diameter were again removed. PPP-A and PPP-B, which were made using similar PPP settings, both exhibited significant porosity in the gage section of each component. PPP-C, which was made with a much higher beam speed and a narrower hatch spacing, showed very little porosity. In general, the porosity content and pore cross sectional area in this experiment was much smaller in comparison to the SS components which is another indication that the parameter settings for the SS components were not optimized for porosity content observed in the various scan strategies. Using the data obtained from the two-dimensional CT slices, approximate fatigue life predictions were calculated for each component, and the components were fatigued until catastrophic failure occurred. Actual fatigue lives and life predictions were then compared (Fig. 5). It was observed that the life was severely underpredicted for each component. This discrepancy indicates that the crack growth model developed by Konecna is not representative of the PPP experiment material. Therefore, AM processing pedigree plays a significant role in crack growth behavior. The components for both the scan strategy study and PPP study were post-processed in the same way, but their original build processing conditions were very different. The SS components were made with almost double the powder layer thickness of the PPP components. This was partially counteracted by increasing the beam power, speed, and hatch spacing for the SS components. Therefore, in order to understand the performance of an AM component it is imperative to also understand the influence of PPPs and scan strategy on microstructure texture and phase development which dictate crack growth behavior.

Further observation indicated that the PPP component fatigue lives were similar to the lives of wrought components subjected to the same loading conditions [22]. Therefore, the crack growth model for a half inch die forged alloy 718 plate subjected to a stress ratio $R = 0.05$ was obtained such that the crack growth constants $(C, n) = (3.0*10^{-13}, 3.89)$. Implementing this new model significantly reduced the error in the life prediction, and pushed each of the predictions to within the 2x scatter band as shown in Fig. 5.

It is also seen in Fig. 5 that PPP-C components significantly outperformed PPP-A and PPP-B components as was hypothesized based on the component porosity size distributions. Additionally, PPP-A and PPP-B appear to perform similarly in regards to the fatigue life. This is consistent with the porosity data shown in Fig. 4 where the CDFs of

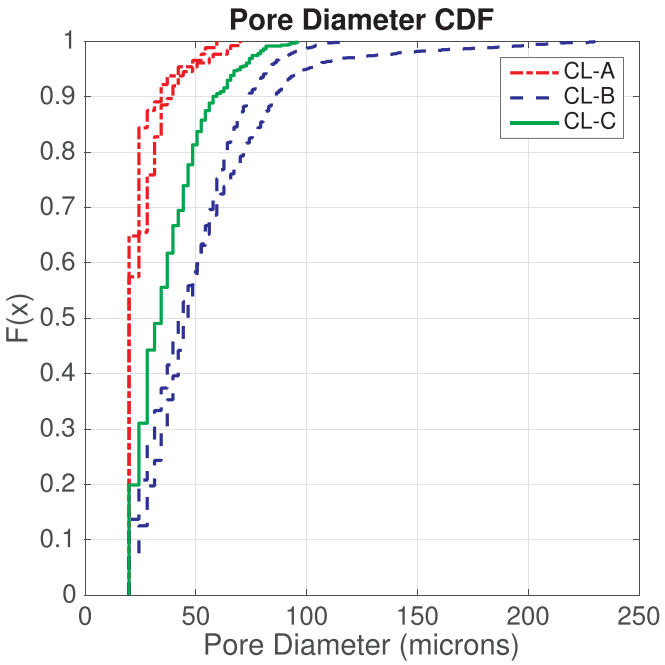

Fig. 2. Cumulative Distribution Function of pore diameter for the SS components.

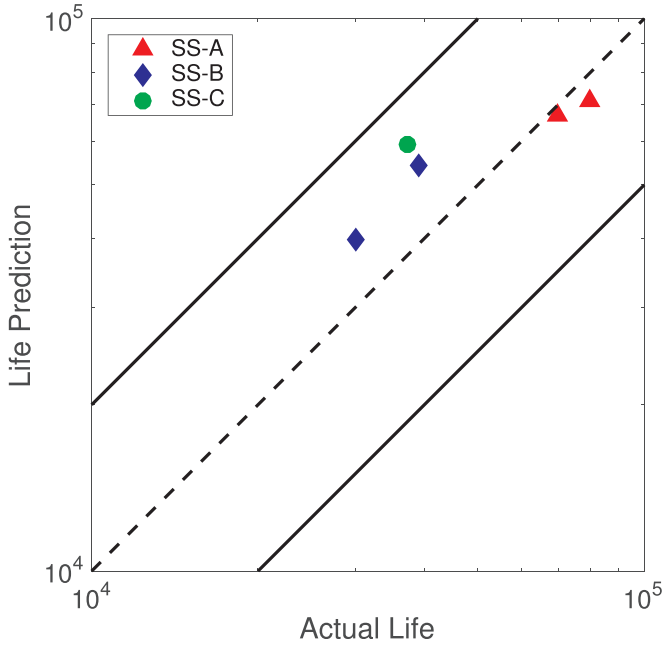

Fig. 3. Life prediction comparison to experimental life for SS components.

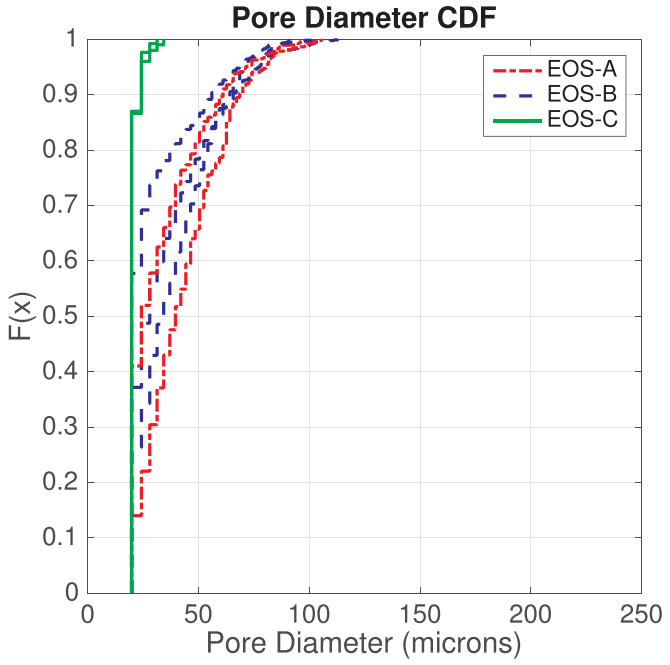

Fig. 4. Cumulative Distribution Function of pore diameter for the PPP components.

porosity diameter for PPP-A and PPP-B components are intermingled with each other. Life prediction of AM components using porosity data from components manufactured via different scan strategies and PPP settings is therefore feasible using two-dimensional data obtained from CT measurements, but pre-existing knowledge of the materials' crack growth behaviors is required to obtain accurate predictions.

3.3. Fractography

The investigation above supports the hypothesis that stress intensities induced by pores of various sizes heavily dictate the fatigue life of a component, and the maximum stress intensity calculated from non-destructive measurements is useful in predicting the fatigue life of additive components following a pre-determined crack growth behavior. To verify the results above, a post-mortem examination of each component's fracture surface was performed.

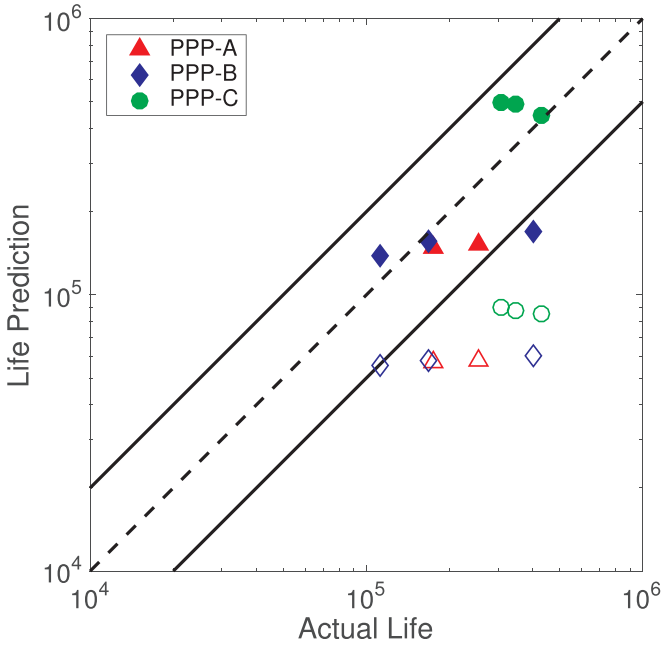

Fig. 5. Life prediction comparison to actual life for PPP components assuming wrought (solid) and previously published AM (empty) crack growth behavior.

Initial observations indicated diverse failure mechanisms among the entire population of components including surface pores, pore lines, and brittle inclusions. Some components did not appear to fail as a result of any of these mechanisms, and further work must be performed to determine the cause of failure. A summary of the failure mechanisms for each component is provided in Table 3, and images of representative crack initiation locations are shown in Fig. 6.

For the five SS components, only two conclusive failure mechanisms were identified. One SS-B component exhibited a large spherical pore at the crack initiation location. Further examination of the entire fracture surface revealed multiple large pores in straight lines which may correspond to a strip intersection location. These anomalies were not observed in the other SS-B component; however a larger number of observations must be made to draw any conclusions as to why the pore lines were present in the component. The second conclusive failure mechanism was a small pore at the surface of SS-C. The elongated pore was very small compared to the pores mentioned before, but the life exhibited by SS-C was nearly the same as SS-B. This could indicate that

Table 3
Summary of fractographic observations and measurements.

PPP setting	Fatigue life	Failure mechanism	Predicted defect size	Observed defect size	Post-failure life prediction
SS-A	69,559	–	70.00	–	–
	79,904	Inclusion	59.39	41.24	44,119
SS-B	29,974	–	230.04	–	–
	39,079	Pore	119.62	53.52	40,340
SS-C	37,167	Pore	95.98	19.72	55,650
PPP-A	254,090	Pore	102.88	43.75	127,550
	175,724	Pore	105.7	39.82	139,700
PPP-B	167,154	Pore	100.96	36.63	151,420
	404,301	–	92.87	–	–
	111,791	Pore	112.87	33.49	165,070
PPP-C	346,635	Other	31.31	–	–
	308,118	Other	–	–	–
	430,679	Other	34.29	–	–

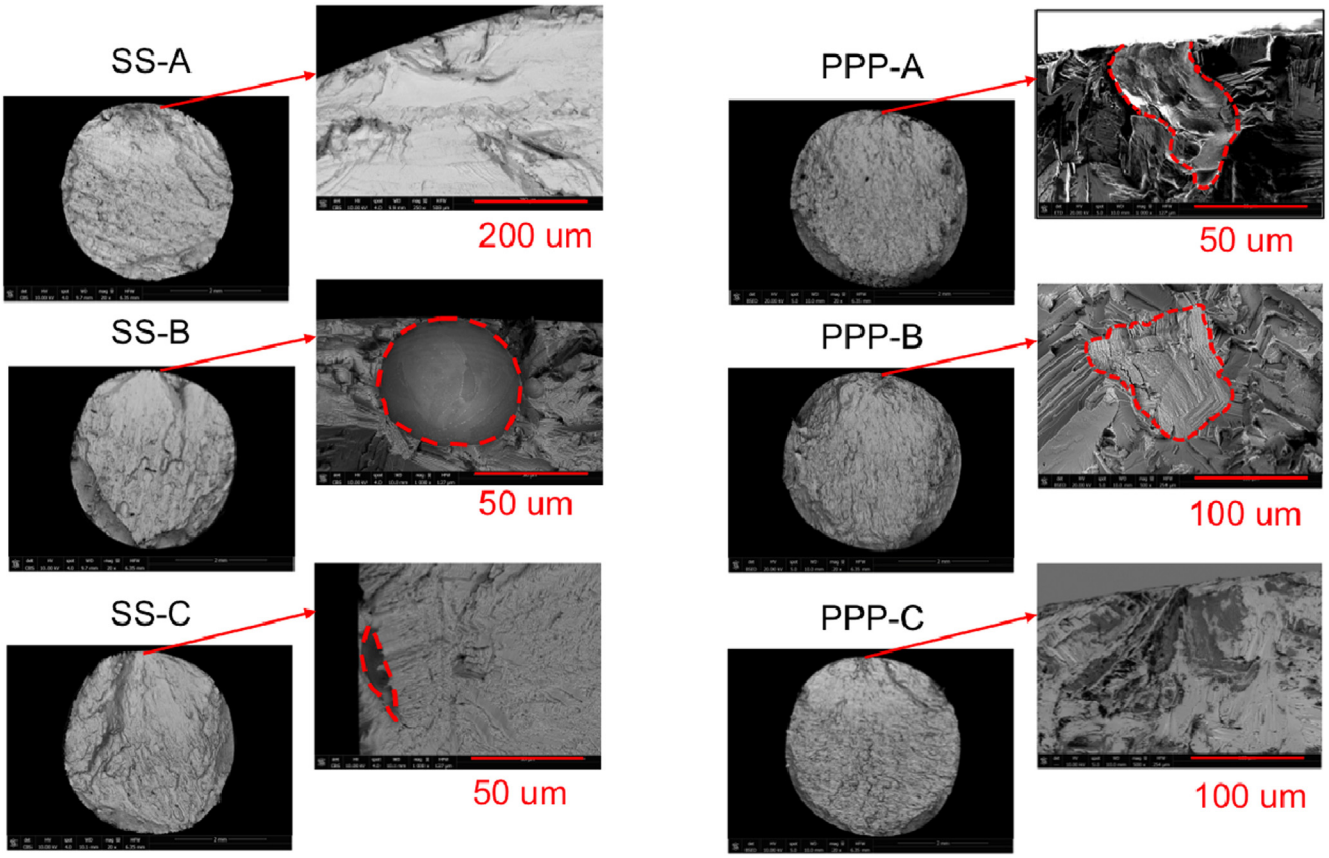

Fig. 6. Fractographs obtained from the crack initiation locations for both experiments.

the pore was partially obscured from view on the fracture surface or that local crack growth behavior was different from the crack growth model. Crack growth experiments will reveal location dependence of crack growth behavior and will shed light on the true crack growth behavior of these components.

For the PPP parts, it was observed that the lowest performing components failed at easily observable pores, but the higher performing components were more ambiguous as to their failure mechanisms. Fig. 6 shows three fractographs each exhibiting a different failure mechanism. One PPP-A component clearly showcases a pore at the initiation location, but the images shown for both PPP-B and PPP-C show ambiguous failure mechanisms. Both experiments showed that the pores observed in the fractographs were typically smaller than those observed in the CT measurements. When the crack growth life prediction approach described above was applied based on the observed fracture surface porosity, the life predictions were different from the CT-based predictions, but they were still within the 2x scatter band (see Fig. 7). The difference between CT-based predictions and fractography-based predictions may have been caused by local crack growth behavior that caused deviations from the model for each scan strategy or PPP setting. This is supported by the observation that components within PPP-A and within PPP-B seemed to exhibit similar failure pore sizes and life predictions. Therefore, initial observations support the claim that components manufactured and processed under the same pedigree will perform at similar levels because they contain similar porosity content. Furthermore, components manufactured and processed under different pedigrees may not perform at the same level because an increase or decrease in porosity, not to mention other microstructural features, will differ, therefore varying the crack growth behavior of the components.

4. Conclusion

The PSPP relationship for AM alloy 718 has been explored by characterizing the development of porosity under different processing conditions and from two different machines. The porosity within each

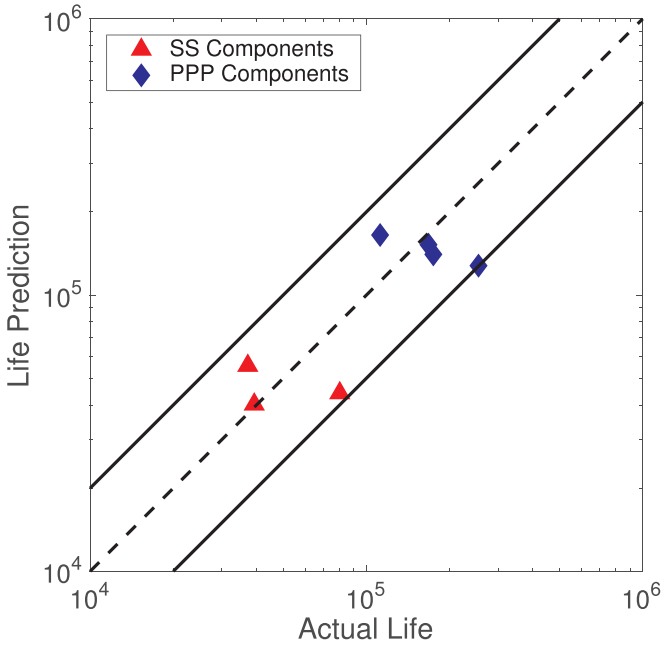

Fig. 7. Fractograph-based life prediction comparisons to actual life for components which failed due to observable defects. Crack growth constants as described above were used for each experiment.

component was measured and analyzed, and the influence of the porosity on the fatigue life of the components was measured which lead to several new insights.

First, scan strategy and primary processing parameters are important factors that dictate the porosity content within AM components. Second, the porosity that is induced by varying scan strategy and primary processing parameters dictates the fatigue life of the machined AM component. Third, non-destructive observation of component porosity can be leveraged to accurately predict fatigue life. It has also been shown that predictions based on CT measurements are similar to predictions based on fracture surface porosity measurements; however, accurate life prediction can only be obtained, if the crack growth data of each material system is known.

This investigation is a “first of its kind” look at the comprehensive relationship between the processing, structure, properties, and performance of AM components with respect to porosity. The results presented here provide significant insight into the behavior of AM materials and represent a leap in understanding of AM processing and material performance that can be used in the design of future components. With this new understanding, AM processes can continue to be optimized for reduction of porosity and improved performance, and design constraints can be developed to account for the intrinsic detriment imposed by internal porosity.

Data availability

The raw/processed data required to reproduce these findings cannot be shared at this time as the data also forms part of an ongoing study.

Acknowledgments

The authors would like to thank the Turbine Engine Fatigue Facility (TEFF) of the United States Air Force Research Laboratory (AFRL) and Universal Technology Corporation (UTC) for funding and support. Additional thanks goes to Maj. Ryan O’Hara and his team at the Air Force Institute of Technology (AFIT) and Colt Montgomery at Carnegie Mellon University who manufactured the components, and to Andy Rosenberger of the Materials and Manufacturing Directorate at AFRL heat treated the components used in this investigation.

References

[1] J. Fielding, R. Gorham, A. Davis, B. Bouffard, K. Morris, Department of Defense Joint Additive Manufacturing Roadmap, 2016.
[2] E. Chlebus, K. Gruber, B. Kuznicka, J. Kurzac, T. Kurzynowski, Effect of heat treatment on the microstructure and mechanical properties of Inconel 718 processed by selective laser melting, Mater. Sci. Eng. A 639 (2015) 647–655.
[3] O. Scott-Emuakpor, C. Holycross, T. George, K. Knapp, J. Beck, Fatigue and strength studies of Titanium 6Al-4V fabricated by direct metal laser sintering, J. Eng. for Gas Turbines and Power, 138.
[4] D. Greitemeier, F. Palm, F. Syassen, T. Melz, Fatigue performance of additive manufactured TiAl6V4 using electron and laser beam melting, Int. J. Fatigue 94 (2017) 211–217.
[5] A. Yadollahi, N. Shamsaei, S.M. Thompson, A. Elwany, L. Bian, Effects of building orientation and heat treatment on fatigue behavior of selective laser melted 17-4 PH stainless steel, Int. J. Fatigue 94 (2017) 218–235.
[6] J. Gockel, L. Sheridan, S.P. Narra, N.W. Klingbeil, J. Beuth, Trends in solidification grain size and morphology for additive manufacturing of Ti-6Al-4V, JOM 69 (12) (2017) 2706–2710.
[7] R.R. Dehoff, M.M. Kirka, F.A. List, K.A. Unocic, W.J. Sames, Crystallographic texture engineering through novel melt strategies via electron beam melting: Inconel 718, Mater. Sci. and Technol, 31 (8).
[8] R.R. Dehoff, M.M. Kirka, W.J. Sames, H. Bilheux, A.S. Tremsin, L.E. Lowe, S.S. Babu, Site specific control of crystallographic grain orientation through electron beam additive manufacturing, Mater. Sci. Technol. 31 (8) (2015) 931–938.
[9] A. Vasinonta, Process maps for predicting residual stress and melt pool size in the laser-based fabrication of thin-walled structures, J. Manuf. Sci. Eng. 129 (1) (2006) 101–109.
[10] R. Cunningham, S.P. Narra, T. Ozturk, J. Beuth, A.D. Rollet, Synchotron-based x-ray microtomography characterization of the effect of processing variables on porosity formation in laser powder-bed additive manufacturing of Ti-6Al-4V, JOM 69 (3) (2017) 765–771.
[11] R. Rashid, S.H. Masood, D. Ruan, S. Palanisamy, R.A.R. Rashid, M. Brandt, Effect of scan strategy on density and metallurgical properties of 17-4PH parts printed by selective laser melting (SLM), J. Mater. Process. (2017) 502–511.
[12] Q. Zhang, Z. Zuo, J. Liu, Numerical analysis for the influence of casting microporosity on fatigue life, Eng. Fail. Anal. 48 (2015) 11–20.
[13] R.A. Hardin, Integrated design of castings: effect of porosity on mechanical performance, Mater. Sci. Eng., A 33.
[14] M. Tiryakioglu, On the relationship between statistical distributions of defect size and fatigue life in 7050-T7451 thick plate and A356-T6 castings, Mater. Sci. Eng. A 520 (2009) 114–120.
[15] T. Miyazaki, H. Kang, H. Noguchi, K. Ogi, Prediction of high-cycle fatigue life reliability of aluminum cast alloy from statistical characteristics of defects at meso-scale, Int. J. Mech. Sci. 50 (2008) 152–162.
[16] ASTM, Standard specification for additive manufacturing nickel alloy (UNS N07718) with powder bed fusion, ASTM Book of Standards.
[17] American Metallurgical Society, Heat Treatment Wrought Nickel Alloy and Cobalt Alloy Parts, 2016.
[18] ASTM, Standard practice for conducting force controlled constant amplitude axial fatigue tests of metallic materials, ASTM Book of Standards.
[19] W.S. Rasband, Imagej, 2017.
[20] Y. Murakami, Metal fatigue: effects of small defects and nonmetallic inclusions, Elsevier Science, 2002, Ch. Stress Concentration, pp. 17–22.
[21] R. Konecna, L. Kunz, G. Nicolletto, A. Baca, Long fatigue crack growth in Inconel 718 produced by selective laser melting, Int. J. Fatigue 92 (2) (2016) 499–506.
[22] Metallic Materials Properties Development and Standardization (MMPDS), 1, 2015.